Physical-priors-guided Aortic Dissection Detection using Non-Contrast-Enhanced CT images

Zhengyao Ding[1], Yujian Hu[2], Hongkun Zhang[2], Fei Wu[1], Shifeng Yang[4], Xiaolong Du[5], Yilang Xiang[2], Tian Li[3], Xuesen Chu[6(✉)], and Zhengxing Huang[1]

[1] Zhejiang University, China {zhengyao.ding,wufei,zhengxinghuang}@zju.edu.cn
[2] The First Affiliated Hospital of Zhejiang University School of Medicine, China {3170103999,1198050,21618130}@zju.edu.cn
[3] The Hong Kong Polytechnic University tianli@polyu.edu.hk
[4] Department of Radiology, Shandong Provincial Hospital Affiliated to Shandong First Medical University, China ysfirst@126.com
[5] Nanjing Drum Tower Hospital, Affiliated Hospital of Medical School, Nanjing University, China dd0341@163.com
[6] China Ship Scientific Research Center chuxs@cssrc.com.cn

Abstract. Aortic dissection (AD) is a severe cardiovascular emergency requiring prompt and precise diagnosis for better survival chances. Given the limited use of Contrast-Enhanced Computed Tomography (CE-CT) in routine clinical screenings, this study presents a new method that enhances the diagnostic process using Non-Contrast-Enhanced CT (NCE-CT) images. In detail, we integrate biomechanical and hemodynamic physical priors into a 3D U-Net model and utilize a transformer encoder to extract superior global features, along with a cGAN-inspired discriminator for the generation of realistic CE-CT-like images. The proposed model not only innovates AD detection on NCE-CT but also provides a safer alternative for patients contraindicated for contrast agents. Comparative evaluations and ablation studies against existing methods demonstrate the superiority of our model in terms of recall, AUC, and F1 score metrics standing at 0.882, 0.855, and 0.829, respectively. Incorporating physical priors into diagnostics offers a significant, nuanced, and non-invasive advancement, seamlessly integrating medical imaging with the dynamic aspects of human physiology. Our code is available at https://github.com/Yukui-1999/PIAD.

Keywords: Physical-priors-guided · Aortic dissection · NCE CT

1 Introduction

Aortic dissection (AD) is a relatively uncommon yet potentially fatal condition, where the patient's aorta is split into a true lumen and a false lumen due to a

---

First Author and Second Author contribute equally to this work.

tear. Rupture of these lumens often results in fatal outcomes [15]. The complexity of its symptoms underscores the importance of accurate diagnosis to avoid severe outcomes [18]. The gold standard for AD diagnosis is Contrast-Enhanced Computed Tomography (CE-CT), acclaimed for its exceptional sensitivity and specificity, exceeding 95% [3]. This superior diagnostic performance is attributed to the contrast agent's X-ray attenuation coefficient, which significantly exceeds that of the vessel wall, facilitating distinct delineation in CE-CT. Nonetheless, CE-CT is not a routine examination in clinical screening scenarios, and the use of a contrast agent in CE-CT comes with potential risks, particularly for individuals with allergies or those suffering from acute renal failure [2]. Therefore, many patients, particularly those exhibiting symptoms akin to AD that overlap with other cardiovascular ailments, are initially evaluated via Non-Contrast-Enhanced CT (NCE-CT). However, as shown in Fig.1, the diagnostic dilemma with NCE-CT lies in the minimal contrast between the aorta and the intimal flap, which obscures the diagnosis of AD and heightens the likelihood of misdiagnosis [10]. In

(a) Contrast-Enhanced Computed Tomography (CE-CT)   (b) Non-Contrast-Enhanced CT (NCE-CT)
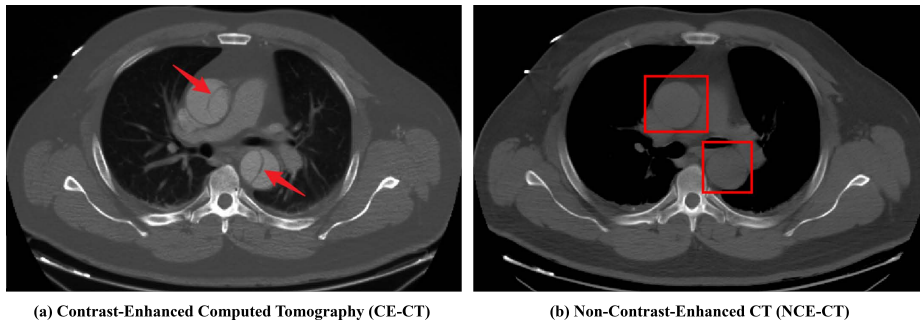
Fig. 1: A patient with aortic dissection (AD): The dissection is visible in the CE-CT, but identifying the dissection in the corresponding NCE-CT is challenging.

response to this challenge, many methods have been proposed for distinguishing AD from non-AD cases, utilizing 2D axial NCE-CT images [11], 3D NCE-CT volumes and morphologic characteristics [27], or synthesized CE-CT images from NCE-CT scans [26,25]. The discussed methods originate from CT image pixels and use convolutional feature extraction to detect AD. However, given the intricate biomechanical and hemodynamic complexities inherent in the cardiovascular system [19], we argue that traditional pixel-based approaches may not fully capture the comprehensive range of factors involved in AD. Dillon-Murphy et al. [7] and Allen at al. [1] used Computational Fluid dynamics (CFD) and 4D flow to obtain hemodynamic parameters in aortic dissection respectively and compared them with a control group. The results indicated that patients suffering from AD had a significant increase in blood flow pulse pressure and flow velocity. Indeed, the physical conditions of blood flow critically determine the aortic wall's dynamics, influencing AD's appearance in imaging modalities [24].

Based on the above findings, it is essential to incorporate physical priors that reflect the actual environmental conditions into the diagnostic paradigm. This can provide a more holistic understanding of the factors contributing to AD, thereby enhancing the accuracy and reliability of AD diagnosis. In light of this, our study
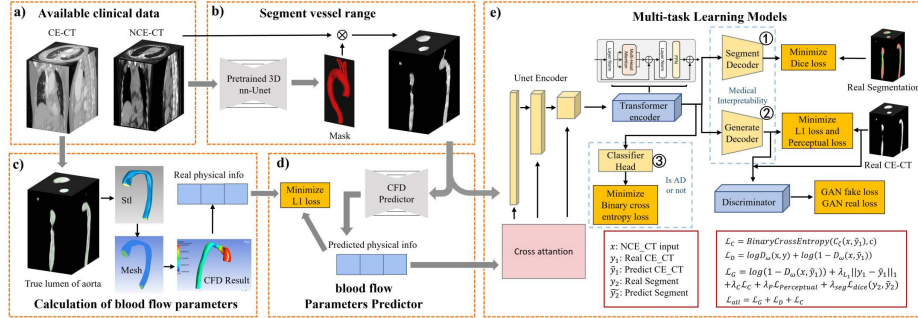

Fig. 2: The framework of our proposed PIAD (Physically Informed Aortic Dissection Detection). (a) Data Collection and Preprocessing, (b) Blood Vessel Segmentation utilizing a 3D U-Net convolutional neural network, (c) Calculation of Blood Flow Parameters via ANSYS Fluent, (d) Prediction of Blood Flow Parameters employing a dedicated neural network, and (e) Our proposed model designed for segmentation, generation and classification tasks, simultaneously.

presents a novel framework that integrates physical prior information for identifying AD through an alternative modality. The primary contributions of our study are threefold: **(i)** To address the high costs and potential risks associated with CE-CT, we propose a novel method that solely utilizes NCE-CT for detection. This approach incorporates the tasks of true and false lumen segmentation and CE-CT synthesis within the framework to aid in aortic dissection detection, thereby enhancing AD detection performance. **(ii)** We introduce physical priors specifically designed to encapsulate the influence of physical factors on AD detection, offering a more comprehensive understanding of the disease diagnosis. To the best of our knowledge, it's the first work to use physical prior knowledge of hemodynamics for AD detection. **(iii)**Experimental results from three datasets confirm our model's superior AD detection in CT images, with ablation studies highlighting the importance of physical priors for improved efficacy.

2 Method

2.1 3D Aorta Segmentation

To focus on the aortic region in CT images, we segment the aorta using a pre-trained nnUnet network [12,13], accurately extracting the aortic mask from NCE-CT images, as shown in Fig.2(b). Subsequent experiments are conducted based on the segmented aorta.
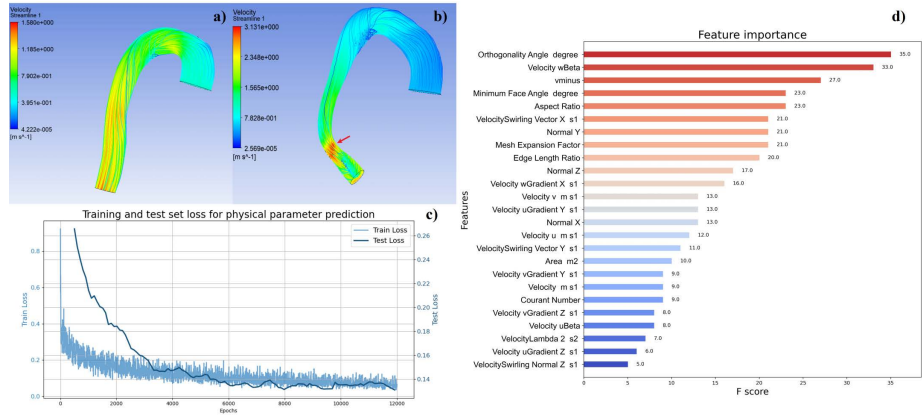
Fig. 3: a) Velocity flow field without dissection. b) Velocity flow field with dissection, the arrow indicates the local maximum caused by the dissection. c) Training set loss and test set loss for the CFD-predictor model. d) Feature importance values of physical information parameters obtained using XGBoost.

2.2   Blood Flow Parameter Calculation

To incorporate hemodynamic parameters into our model, we used Computational Fluid dynamics (CFD) to calculate the flow field in the true lumen of the patient's aorta and then used a neural network to predict the CFD result, since there was no label of the true lumen in the inference stage.

The pipeline for calculating hemodynamic parameters using ANSYS Fluent is illustrated in Fig.2(c), which begins with using Mimics-19 to isolate the aortic true lumen from the scans, simplifying the vessel's geometry by removing aortic arch branches and smoothing the surface. The STL file from Mimics is refined in Geomagic Studio, segmenting the vessel into inlets and outlets and optimizing mesh size for fluid dynamics simulations. This refined STL is processed in ICEM CFD for mesh generation, followed by importing the mesh into CFX-Pre to set blood flow parameters: steady-state, density: $1066\,\mathrm{kg\cdot m^{-3}}$, viscosity: $0.0035\,\mathrm{Pa\cdot s}$, relative pressure: $9490\,\mathrm{Pa}$, inlet velocity: $0.5\,\mathrm{m\cdot s^{-1}}$, and outlet pressure: $0\,\mathrm{Pa}$ for simulations in ANSYS Fluent, generating comprehensive hemodynamic data. The obtained results comprise a series of physical parameters for each point within the blood vessel. Next, given the diverse and potentially redundant blood flow parameters obtained from ANSYS Fluent, we employed XGBoost [6] for AD classification, selecting the three most important features as the physical parameters to be embedded into the main model. To reduce the complexity of the subsequent prediction network, we used the ratio of the maximum to minimum values of each parameter in space as the representative value of that physical information. For inference without direct true lumen access, we predicted these parameters using a 3D UNet [20] and Transformer encoder [23] network on NCE-CT images, which was trained by L1 loss (as shown in Fig.2(d)). This approach

enhances our model's practicality for real-world application by estimating crucial hemodynamic parameters without direct measurements.

2.3 3D Physical-guided Model

Our primary model PIAD (Physically Informed Aortic Dissection Detection), depicted in Fig.2(e), incorporates true and false lumen segmentation tasks and CE-CT generation tasks, enabling the encoder to learn more features and thereby improving AD detection performance. The original CT data x first passes through an encoder guided by the predicted physical information parameters through cross-attention [23] (See supplementary materials for details). The output is passed through a Transformer encoder to capture the global information of the CT data [5,22]. Next, the output of the transformer encoder t is then fed into the classification head for classification, a decoder for generating CE-CT data, and another decoder for segmenting true and false lumens. The classification loss is $\mathcal{L}_C = \text{BinaryCrossEntropy}\Big(C_{\zeta_C}(t), c\Big)$, where c is the label of AD. Each layer of these two decoders also receives data from each layer of the preceding UNet encoder, forming skip connections. For segment and generation tasks, we define y_1: the real CE-CT image, y_2: real segment image, $\tilde{y}_1$: predicted CE-CT image, $\tilde{y}_2$: predicted segment image, G: the whole encoder and two decoder, D: the discrimination of GANs [9]. Then the loss of the generator is $\mathcal{L}_G = \log(1 - D_\omega(x, \tilde{y}_1)) + \lambda_{L_1}||y_1 - \tilde{y}_1||_1 + \lambda_P \mathcal{L}_P + \lambda_C \mathcal{L}_C + \lambda_{seg} \mathcal{L}_{dice}(y_2, \tilde{y}_2)$, where the $\mathcal{L}_P$ is perceptual loss via a pre-trained VGG network, the $\mathcal{L}_C$ is the classification loss obtained after fixing the classifier. The loss of the discrimination is $\mathcal{L}_D = log D_\omega(\text{x}, \text{y}) + log\big(1 - D_\omega(x, \tilde{y}_1)\big)$. Thus, the total loss function is $\mathcal{L}_{all} = \mathcal{L}_G + \mathcal{L}_D + \mathcal{L}_C$.

3 Experiments

3.1 Datasets and Experiment Details

The training and internal testing dataset included 250 preoperative subjects (117 AD and 133 non-AD patients) from the First Affiliated Hospital of Zhejiang University School of Medicine, with additional external datasets (only for verification) from Shandong Provincial Hospital Affiliated to Shandong First Medical University and Nanjing Drum Tower Hospital, each comprising 25 AD and non-AD patients. Preprocessing involved B-spline non-rigid registration between NCE-CT and CE-CT, resampling to $1.3 \times 1.3 \times 5mm^3$, and cropping to $128 \times 128 \times 64$ around the thoracic aorta. CT values were clipped to [0,200] for NCE-CT and [0,800] for CE-CT, with normalization to [-1,1]. We used five-fold cross-validation for evaluation, training the physical prediction model with Adam for 100 epochs, starting at 1e-5 and decaying to 0 after 50 epochs. The main model, trained on a 24 GB NVIDIA GeForce RTX 4090 GP for 200 epochs, used different learning rates (1e-5, 1e-4, and 1e-5) for the generator, discriminator, and classifier, reducing to 0 over 100 epochs. The loss weights $\lambda_{L_1}, \lambda_P, \lambda_C$, and λ_{seg} mentioned in Subsection 2.3 were set to 10, 10, 10, and 100, respectively.

3.2   Results

Hemodynamic Parameter Results: Fig.3(a) and Fig.3(b) portray the velocity flow field of the aorta in the presence and absence of aortic dissection, respectively. Notably, the presence of a dissection results in a local maximum in the flow field at the narrowed true lumen, which generally represents the overall maximum within the entire flow field. This disparity leads to a notable increase in the variation between maximum and minimum physical quantities compared to cases without dissection, thereby enhancing subsequent model training.

The CFD computation yielded blood flow parameters across 71 categories. To address the issue of potential information redundancy, we utilized XGBoost to perform a feature importance ranking. The results, focusing on the top 10 features for clarity, are presented in Fig.3(d). We selected the top three ranked parameters for training the main model. Given the absence of real true lumen labels during the inference stage, we employed a neural network to predict the calculated physical parameters. The training and test loss curves, illustrated in Fig.3(c), demonstrate the models' capability to reasonably fit the physical parameters obtained from CFD calculations to a certain extent. Building upon this, we used the predicted physical information into the main model to enhance its performance in tasks such as AD detection. The final results are as follows.

Table 1: Comparison results between previous methods and our method.

		Single tasks methods					Multi tasks methods			
		RegGAN	3D Pix2Pix	MedNext	3D nnU-net	ADXception	ViT backbone	SwinT backbone	3D MTGA	PIAD(Ours)
	SSIM ↑	0.960±0.002	0.933±0.003	/	/		0.931±0.011	0.948±0.009	0.944±0.015	**0.963±0.004**
	PSNR ↑	**33.455±1.283**	31.189±2.605	/	/		31.245±1.245	32.482±1.420	32.317±0.411	33.393±3.773
	DSC ↑	/	/	0.606±0.010	0.497±0.029		0.455±0.023	0.564±0.024	0.519±0.048	**0.625±0.015**
	Jaccard ↑	/	/	0.532±0.15	0.428±0.026		0.402±0.012	0.510±0.019	0.433±0.061	**0.574±0.011**
Internal	Acc ↑	/	/	/	/	0.805±0.012	0.796±0.010	0.810±0.025	0.801±0.080	**0.837±0.045**
Dataset	Prec ↑	/	/	/	/	0.765±0.025	0.759±0.015	0.795±0.092	0.756±0.120	**0.790±0.083**
	Recall ↑	/	/	/	/	0.869±0.096	0.825±0.024	0.870±0.010	0.862±0.091	**0.882±0.076**
	Spec ↑	/	/	/	/	0.760±0.012	0.738±0.018	0.765±0.032	0.750±0.107	**0.784±0.074**
	AUC ↑	/	/	/	/	0.810±0.050	0.804±0.032	0.825±0.009	0.838±0.073	**0.855±0.058**
	F1 ↑	/	/	/	/	0.785±0.040	0.775±0.028	0.809±0.025	0.799±0.083	**0.829±0.055**

		Single tasks methods			Multi tasks methods			
		RegGAN	3D Pix2Pix	ADXception	ViT backbone	SwinT backbone	3D MTGA	PIAD(Ours)
	SSIM ↑	0.956±0.003	0.920±0.001	/	0.926±0.008	0.942±0.012	0.935±0.020	**0.969±0.006**
	PSNR ↑	35.285±0.940	31.102±0.765	/	31.894±1.450	32.902±1.225	33.975±0.644	**35.435±3.813**
	Acc ↑	/	/	**0.830±0.028**	0.801±0.012	0.815±0.042	0.821±0.058	0.819±0.060
External	Prec ↑	/	/	0.781±0.025	0.758±0.061	0.769±0.077	0.782±0.050	**0.790±0.045**
Dataset 1	Recall ↑	/	/	0.879±0.021	0.858±0.043	0.870±0.038	0.859±0.074	**0.889±0.059**
	Spec ↑	/	/	**0.795±0.019**	0.756±0.090	0.770±0.041	0.751±0.131	0.779±0.112
	AUC ↑	/	/	0.879±0.038	0.847±0.031	0.871±0.035	0.878±0.024	**0.889±0.035**
	F1 ↑	/	/	0.826±0.017	0.807±0.062	0.810±0.011	0.819±0.025	**0.828±0.047**
	SSIM ↑	**0.962±0.009**	0.904±0.001	/	0.919±0.010	0.936±0.005	0.926±0.018	0.960±0.008
	PSNR ↑	35.015±1.124	30.478±0.720	/	32.012±1.980	33.849±2.203	33.016±0.354	**35.021±3.215**
	Acc ↑	/	/	**0.815±0.041**	0.788±0.029	0.798±0.040	0.811±0.062	0.801±0.069
External	Prec ↑	/	/	0.780±0.031	0.762±0.040	0.779±0.077	0.775±0.060	**0.782±0.062**
Dataset 2	Recall ↑	/	/	0.868±0.034	0.835±0.029	0.852±0.084	0.848±0.054	**0.874±0.045**
	Spec ↑	/	/	0.759±0.080	0.735±0.010	0.746±0.067	0.738±0.106	**0.770±0.121**
	AUC ↑	/	/	0.875±0.012	0.853±0.059	0.870±0.073	0.876±0.020	**0.883±0.035**
	F1 ↑	/	/	0.810±0.071	0.789±0.015	0.805±0.040	0.807±0.020	**0.818±0.065**

Main Results: (1) Baselines: We compare our PIAD with existing popular and state-of-the-art (SOTA) methods, categorized by tasks into four types:
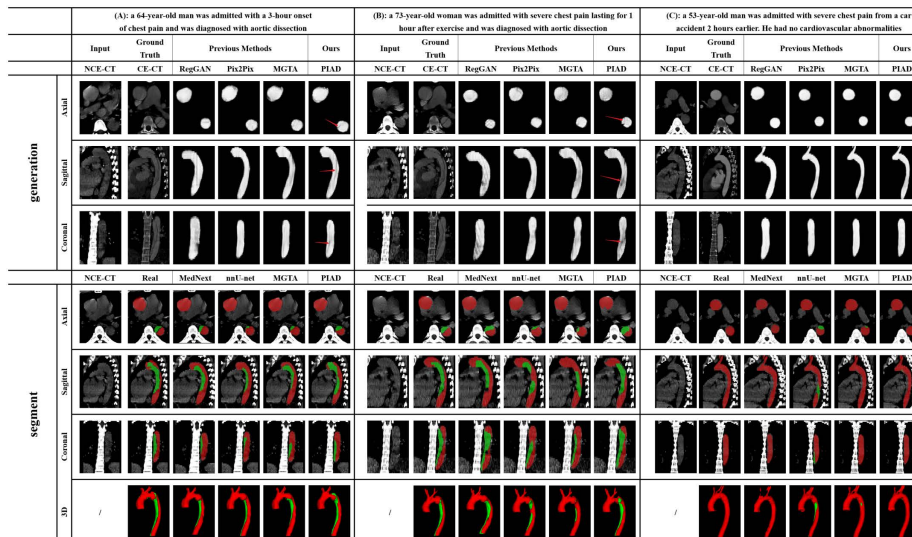
Fig. 4: Visualisations of generation and segmentation experiments adopting various strategies. Rows from top to bottom are different views for segment and generation tasks. For each patient, columns from left to right are the input NCE-CT image, ground truth, results adopting previous methods, and our proposed PIAD.

Single-generation tasks: Pix2Pix [14], RegGAN [16]; **Single-segmentation tasks**: 3D nnU-net [12], Mednext [21]; **Single-classification tasks**: ADXception [11]; **Multiple tasks**: Vision Transformer [8] backbone, Swin Transformer [17] backbone, 3D MGTA [25]. **(2) Evaluation Metrics:** For generative tasks, we use SSIM and PSNR to evaluate similarity. Segmentation tasks are assessed using the DSC and Jaccard index, while classification tasks are measured with Sens, Spec, Prec, F1 score, AUC, and ACC. **Notably, previous single-task baselines are specially designed for specific tasks, where we can only evaluate the model performance on the corresponding metrics.** The results outlined in Table 1 indicate that our proposed PIAD consistently outperforms previous methods in both multi-task and single-task settings, underscoring the advantages of leveraging physical information and a multi-task learning strategy. These findings validate the model's superior accuracy and efficacy. **Notably, the external datasets do not include labels for segmentation, hence a comparison of segmentation performance was not conducted.**

Visual Results: The qualitative results of the generation and segmentation are depicted in Fig.4. Notably, our model achieves superior generation and segmentation effects in the NCE-CT images of patients with AD as well as in healthy individuals. These outcomes hold significant value for radiologists in diagnosing AD and also serve as compelling evidence of the model's interpretability.

3.3   Ablation Studies

We conducted ablation studies with the following variants: **W/O Physics**, which denotes the model's performance without the embedding of physical information; **W/O Transformer**, indicating the model's performance without utilizing a Transformer encoder to capture long-range dependencies; **Cascade Classifier**, which refers to the model's performance when segmentation and generation results are cascaded (sequentially) rather than parallel to the classifier; **Single Generation, Single Segment, and Single Classification** represent the model's performance when we focus exclusively on a single task, by only training the single-task decoder and freezing decoders for other tasks. Table 2

Table 2: Ablation Studies

	W/O Physics	W/O Transformer	Cascade Classifier	Single Generation	Single Segment	Single Classification	PIAD(Ours)
SSIM ↑	0.961±0.004	0.949±0.031	0.967±0.003	0.955±0.006	/	/	**0.963±0.004**
PSNR ↑	31.161±3.353	32.394±2.992	31.664±4.466	32.894±2.010	/	/	**33.393±3.773**
DSC ↑	0.624±0.017	0.617±0.021	0.619±0.025	/	0.595±0.286	/	**0.625±0.015**
Jaccard ↑	0.574±0.012	0.503±0.151	0.505±0.153	/	0.530±0.224	/	**0.574±0.011**
Acc ↑	0.814±0.077	0.805±0.004	0.801±0.004	/	/	0.785±0.032	**0.837±0.045**
Prec ↑	0.772±0.104	0.747±0.005	0.780±0.002	/	/	0.754±0.080	**0.790±0.083**
Recall ↑	0.854±0.075	0.870±0.005	0.792±0.024	/	/	0.820±0.078	**0.882±0.076**
Spec ↑	0.753±0.099	0.750±0.004	0.803±0.008	/	/	0.745±0.075	**0.784±0.074**
AUC ↑	0.840±0.075	0.830±0.006	0.849±0.005	/	/	0.801±0.050	**0.855±0.058**
F1 ↑	0.808±0.079	0.803±0.005	0.779±0.008	/	/	0.768±0.105	**0.829±0.055**

reveals that models incorporating physical information embedding exhibit enhanced AD detection, along with improved generation and segmentation performance. Additionally, incorporating a transformer encoder facilitates the model in extracting global features over extended distances. Furthermore, two main drawbacks are evident in the prevailing MTGA [25], where segmentation tasks, generation tasks, and final AD detection tasks are sequentially interconnected. Firstly, classifying based on generated content may lead to the loss of some information present in the original image. Secondly, the segmentation task may confine the model's attention solely to the true and false lumen areas, potentially overlooking crucial features such as aortic dilation. The single-task experiments in Table 2 further validate that our model's parallel processing of segmentation, generation, and classification tasks leverages a shared encoder to refine the semantic encoding space. This approach addresses the limitations above and elevates the overall efficacy of the model.

4   Conclusion and Discussion

This study introduces a method that incorporates physical information to enhance the detection of Aortic Dissection. By integrating physical data that reflects the condition of the aorta, our model demonstrates improved diagnostic capabilities, validated through a comprehensive evaluation across three datasets. This advancement signifies a major leap in AD detection technology and its potential for clinical application. One aspect of its clinical significance is that our

model enables the early screening of patients with aortic dissection using NCE-CT, akin to the paper [4]. Additionally, it facilitates the optimization of hospital diagnostic procedures, enabling the swift and accurate identification of aortic dissection over other cardiovascular diseases with similar symptoms. However, it is noteworthy that certain patients presenting with symptoms of limb or back pain—a less common manifestation of aortic dissection—may encounter limitations when diagnosed using NCE-CT. In essence, our research makes a pivotal contribution by leveraging real-world physical properties to improve the performance of downstream tasks, showcasing the potential of integrating physical insights into AI models. This approach not only enhances medical applications but also exemplifies the fusion of AI and science, paving the way for further exploration of physical priors in computational tasks.

Disclosure of Interests. The authors have no competing interests to declare that are relevant to the content of this article.

References

1. Allen, B.D., Aouad, P.J., Burris, N.S., Rahsepar, A.A., Jarvis, K.B., François, C.J., Barker, A.J., Malaisrie, S.C., Carr, J.C., Collins, J.D., et al.: Detection and hemodynamic evaluation of flap fenestrations in type b aortic dissection with 4d flow mri: comparison with conventional mri and ct angiography. Radiology: Cardiothoracic Imaging **1**(1), e180009 (2019)
2. Alter, S.M., Eskin, B., Allegra, J.R.: Diagnosis of aortic dissection in emergency department patients is rare. Western Journal of Emergency Medicine **16**(5), 629 (2015)
3. Braverman, A.C.: Acute aortic dissection: clinician update. Circulation **122**(2), 184–188 (2010)
4. Cao, K., Xia, Y., Yao, J., Han, X., Lambert, L., Zhang, T., Tang, W., Jin, G., Jiang, H., Fang, X., et al.: Large-scale pancreatic cancer detection via non-contrast ct and deep learning. Nature medicine pp. 1–11 (2023)
5. Chen, J., Lu, Y., Yu, Q.T.: Transformers make strong encoders for medical image segmentation. arxiv 2021. arXiv preprint arXiv:2102.04306
6. Chen, T., Guestrin, C.: Xgboost: A scalable tree boosting system. In: Proceedings of the 22nd acm sigkdd international conference on knowledge discovery and data mining. pp. 785–794 (2016)
7. Dillon-Murphy, D., Noorani, A., Nordsletten, D., Figueroa, C.A.: Multi-modality image-based computational analysis of haemodynamics in aortic dissection. Biomechanics and modeling in mechanobiology **15**, 857–876 (2016)
8. Dosovitskiy, A., Beyer, L., Kolesnikov, A., Weissenborn, D., Zhai, X., Unterthiner, T., Dehghani, M., Minderer, M., Heigold, G., Gelly, S., et al.: An image is worth 16x16 words: Transformers for image recognition at scale. arXiv preprint arXiv:2010.11929 (2020)

9. Goodfellow, I., Pouget-Abadie, J., Mirza, M., Xu, B., Warde-Farley, D., Ozair, S., Courville, A., Bengio, Y.: Generative adversarial nets. Advances in neural information processing systems **27** (2014)

10. Harris, R.J., Kim, S., Lohr, J., Towey, S., Velichkovich, Z., Kabachenko, T., Driscoll, I., Baker, B.: Classification of aortic dissection and rupture on post-contrast ct images using a convolutional neural network. Journal of Digital Imaging **32**(6), 939–946 (2019)

11. Hata, A., Yanagawa, M., Yamagata, K., Suzuki, Y., Kido, S., Kawata, A., Doi, S., Yoshida, Y., Miyata, T., Tsubamoto, M., et al.: Deep learning algorithm for detection of aortic dissection on non-contrast-enhanced ct. European radiology **31**, 1151–1159 (2021)

12. Isensee, F., Jaeger, P.F., Kohl, S.A., Petersen, J., Maier-Hein, K.H.: nnu-net: a self-configuring method for deep learning-based biomedical image segmentation. Nature methods **18**(2), 203–211 (2021)

13. Isensee, F., Jäger, P.F., Kohl, S.A., Petersen, J., Maier-Hein, K.H.: Automated design of deep learning methods for biomedical image segmentation. arXiv preprint arXiv:1904.08128 (2019)

14. Isola, P., Zhu, J.Y., Zhou, T., Efros, A.A.: Image-to-image translation with conditional adversarial networks. In: Proceedings of the IEEE conference on computer vision and pattern recognition. pp. 1125–1134 (2017)

15. Karthikesalingam, A., Holt, P., Hinchliffe, R.J., Thompson, M.M., Loftus, I.M.: The diagnosis and management of aortic dissection. Vascular and endovascular surgery **44**(3), 165–169 (2010)

16. Kong, L., Lian, C., Huang, D., Hu, Y., Zhou, Q., et al.: Breaking the dilemma of medical image-to-image translation. Advances in Neural Information Processing Systems **34**, 1964–1978 (2021)

17. Liu, Z., Lin, Y., Cao, Y., Hu, H., Wei, Y., Zhang, Z., Lin, S., Guo, B.: Swin transformer: Hierarchical vision transformer using shifted windows. In: Proceedings of the IEEE/CVF international conference on computer vision. pp. 10012–10022 (2021)

18. Patel, P.D., Arora, R.R.: Pathophysiology, diagnosis, and management of aortic dissection. Therapeutic advances in cardiovascular disease **2**(6), 439–468 (2008)

19. Pollock, J.D., Murray, I., Bordes, S.J., Makaryus, A.N.: Physiology, cardiovascular hemodynamics (2017)

20. Ronneberger, O., Fischer, P., Brox, T.: U-net: Convolutional networks for biomedical image segmentation. In: Medical Image Computing and Computer-Assisted Intervention–MICCAI 2015: 18th International Conference, Munich, Germany, October 5-9, 2015, Proceedings, Part III 18. pp. 234–241. Springer (2015)

21. Roy, S., Koehler, G., Ulrich, C., Baumgartner, M., Petersen, J., Isensee, F., Jaeger, P.F., Maier-Hein, K.H.: Mednext: transformer-driven scaling of convnets for medical image segmentation. In: International Conference on Medical Image Computing and Computer-Assisted Intervention. pp. 405–415. Springer (2023)

22. Valanarasu, J.M.J., Oza, P., Hacihaliloglu, I., Patel, V.M.: Medical transformer: Gated axial-attention for medical image segmentation. In: Medical Image Computing and Computer Assisted Intervention–MICCAI 2021: 24th International Conference, Strasbourg, France, September 27–October 1, 2021, Proceedings, Part I 24. pp. 36–46. Springer (2021)

23. Vaswani, A., Shazeer, N., Parmar, N., Uszkoreit, J., Jones, L., Gomez, A.N., Kaiser, Ł., Polosukhin, I.: Attention is all you need. Advances in neural information processing systems **30** (2017)

24. Williams, J.G., Marlevi, D., Bruse, J.L., Nezami, F.R., Moradi, H., Fortunato, R.N., Maiti, S., Billaud, M., Edelman, E.R., Gleason, T.G.: Aortic dissection is determined by specific shape and hemodynamic interactions. Annals of Biomedical Engineering **50**(12), 1771–1786 (2022)
25. Xiong, X., Ding, Y., Sun, C., Zhang, Z., Guan, X., Zhang, T., Chen, H., Liu, H., Cheng, Z., Zhao, L., et al.: A cascaded multi-task generative framework for detecting aortic dissection on 3-d non-contrast-enhanced computed tomography. IEEE Journal of Biomedical and Health Informatics **26**(10), 5177–5188 (2022)
26. Xiong, X., Guan, X., Sun, C., Zhang, T., Chen, H., Ding, Y., Cheng, Z., Zhao, L., Ma, X., Xie, G.: A cascaded deep learning framework for detecting aortic dissection using non-contrast enhanced computed tomography. In: 2021 43rd Annual International Conference of the IEEE Engineering in Medicine & Biology Society (EMBC). pp. 2914–2917. IEEE (2021)
27. Yi, Y., Mao, L., Wang, C., Guo, Y., Luo, X., Jia, D., Lei, Y., Pan, J., Li, J., Li, S., et al.: Early detection of aortic dissection on non-contrast ct: The combination of deep learning and morphologic characteristics (2021)